Source Localization Using Ultrasonic Lamb Waves with a Least Mean Squares Method

Daewon Kim[1]

[1] *Professor, Department of Applied Computer Engineering, Dankook University,
152 Juk-Jeon-Ro, Su-Ji-Gu, Yong-In-Si, Kyung-Gi-Do, Republic of Korea.*

Abstract

The localization of sources of inhomogeneity is a basic requirement in nondestructive evaluation and subsequent analysis of damage mechanisms. Source localization using various highly effective signal processing schemes have been developed in previous research. In this paper, we localize a defect in an aluminum specimen based on the velocity effect of ultrasonic Lamb waves, measuring the time of flight (TOF) using peak values and then applying a least mean squares algorithm. The mean squared error (MSE) of the measured and simulated distances between the sensors and the defect is minimized using a gradient descent algorithm, which involves moving in a direction opposite to the gradient of the MSE, resulting in the optimal estimation of the x and y coordinates of the defect. The estimated defect location is compared with the actual position of the defect by converting the distance information into real environmental values based on the x and y coordinates. The source localization results depend strongly on the accuracy of the TOF values for the actuator, sensors, and defect. The more precise the TOF information, the better the results.

Keywords: Ultrasound, Lamb waves, Modelling, Source localization, LMS, Gradient descent.

I. INTRODUCTION

The ability to detect, localize, and characterize defects or inhomogeneities in materials is of essential importance. Several nondestructive evaluation (NDE) methods have been developed to test components and structures. Most NDE techniques involve the application of some form of energy to the specimen. A snapshot of the interaction between the material and the energy is taken and analyzed to determine the state of the specimen. The choice of NDE method depends on many factors including the size, orientation, and location of the flaw, as well as the type of material. Guided waves such as ultrasonic Lamb waves are commonly employed to assess a test specimen. Guided waves possess characteristics that those are limited inside the walls of a thin material. These waves generally exist in thin plates with parallel free boundaries, can travel over long distances with little attenuation in different types of material, and can travel within curved walls. These properties mean guided waves are useful for the nondestructive structural health monitoring (SHM) of various objects such as pressure vessels, oil tanks, missiles, aircraft, and pipelines using multiple piezoelectric wafer active sensors (PWASs) and ultrasonic inspection. Horace Lamb first introduced the waves, which are composed of two groups, based on Lord Rayleigh's research in 1917. Generally, ultrasonic Lamb waves are signals of elastic perturbation which propagate in a solid plate without any boundaries [1]. As ultrasonic guided waves, Lamb and shear waves can travel in thin plates. Lamb waves are vertically polarized and symmetric, while shear waves are horizontally polarized and antisymmetric with respect to the mid-plane of the plate. These waves propagate independently of each other, satisfying the boundary conditions and wave equations. Several techniques that employ Lamb waves have been proposed for detecting defects in thin-walled objects. For example, SHM has been conducted based on embedded ultrasonic NDE using PWASs [2] and based on-line evaluation using embedded sensors such as polyvinylidene fluoride (PVDF) film [3]. The ability of embedded PWASs to perform in-situ NDE was explored in [4]. In that research, theoretical developments were used to prove that PWAS transducers can satisfactorily perform the Lamb wave transmission and reception, pulse-echo, pitch-catch, and phased array functions of conventional ultrasonics. In addition, PWAS operating principles and their structural coupling through a thin adhesive layer were analyzed and a model of a Lamb wave tuning mechanism with PWAS transducers was described in [5]. In order to analyze Lamb waves effectively, the measurement of time of flight (TOF) has received particular attention. For source localization using TOF measurements, [6] a number of proposed methods utilize semi-definite programming relaxation. In [7], the ability of embedded PWASs to perform in-situ NDE for the SHM of fiber-reinforced polymer (FRP) composite plates was explored, while [8] investigated the nondestructive sizing and localization of internal micro-cracks in fatigue samples. The latter study described the development and integration of several NDE methods for the monitoring and sizing of micro-cracks in titanium fatigue samples. In that research, ultrasonic Lamb wave signals were continuously excited and acquired within the sample during fatigue tests at different levels of fatigue load using a high-speed data acquisition system.

The maximum likelihood 3-D near-field source localization has been addressed using an expectation-maximization (EM) iterative algorithm to solve the complicated multi-parameter optimization problem associated with 3-D localization [9]. Source location using acoustic emission (AE) can be also be achieved using neural network signal processing based on

arrival time profiles. An artificial neural network-based AE source location method was introduced in [10] that uses signal arrival time profiles that are independent of the material and changes in scale. Defect localization could also be achieved using an orthogonally projected multiple signal classification approach for magnetic flux leakage fields. A multiple signal classification approach has been used to identify defect locations and moments [11]. Another type of source localization is direct joint source localization with propagation speed estimation [12]. This involves the use of the Cramer-Rao bound for joint estimation and the difference in arrival time measured with a sensor array for propagation speed. Source localization and sensing is also possible with nonparametric iterative adaptive approaches based on weighted least squares. A nonparametric and hyper-parameter, free-weighted, least squares-based iterative adaptive approach was presented in [13] for amplitude and phase estimation using array processing. In the present paper, the goal of the research is to identify the location of a defect in a specimen using NDE based on ultrasonic Lamb waves. The velocity of the waves and TOF information are employed to estimate the distance between the sensors and the defect. The mean squared error (MSE) of the measured and simulated distance between the sensors and the defect is then minimized using a least mean squares (LMS) algorithm, resulting in the optimal positioning of the x and y coordinates of the source. The proposed method is tested using ultrasonic Lamb wave signals from both modeling and experiments.

II. ULTRASONIC LAMB WAVES FOR NDE

In solid plates with stress free boundaries, longitudinal and shear waves combine in a specific manner determined by the boundary conditions and stiffness constants of the material, leading to the propagation of elastic Lamb waves, which are sensitive enough to detect multiple defects. Lamb waves can be used to evaluate the cross-section of a specimen. The Lamb waves are generated as being piled one on another of longitudinal and shear modes and exist simultaneously in both symmetric or antisymmetric modes. Figure 1 presents a typical example of Lamb wave generation in a solid plate.
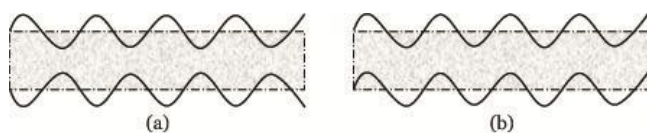

Figure 1. Two forms of Lamb wave: (a) symmetric and (b) antisymmetric

$$\frac{tan(N\times d)}{tan(M\times d)} = \frac{4(MN)i^2}{(i^2-N^2)^2} \tag{1}$$

$$\frac{tan(N\times d)}{tan(M\times d)} = \frac{(i^2-N^2)^2}{4(MN)i^2} \tag{2}$$

Symmetric and the antisymmetric Lamb waves can be formulated mathematically as equations (1) and (2), respectively [14]: where $M^2 = \frac{f^2}{V_L^2} - i^2$, $N^2 = \frac{f^2}{V_T^2} - i^2$, $i = \frac{f}{V_P}$, and $i, d, f, V_P, V_L,$ and V_T are the wave number, plate thickness, wave circular frequency, phase velocity, longitudinal

wave velocity, and transversal wave velocity, respectively. Lamb waves are generated with an infinite number of modes for both symmetric and antisymmetric displacements within the layer. The symmetric modes are referred to as longitudinal modes because the average displacement over the thickness of the plate or layer is in the longitudinal direction, while the antisymmetric modes exhibit average displacement in the transverse direction. An infinite number of modes exists for a specific plate thickness and acoustic frequency, which are identified by their respective phase velocities. The conventional method for describing propagation characteristics is the use of dispersion curves based on plate mode phase velocity as a function of the product of frequency and thickness. The dispersion curves are typically labeled S0, A0, S1, A1 and so on depending on whether the mode is symmetric or antisymmetric. Ideally, a specific working frequency will be found so that the created signals do not distract in space during the NDE process. This optimal frequency can be identified using assays and an analysis of group and phase velocity dispersion curves for aluminum plates (Fig. 2 and Fig. 3, respectively).
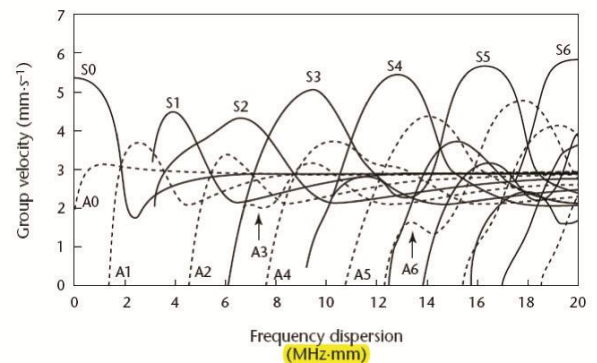

Figure 2. Group velocity dispersion curves for Lamb waves in an aluminum plate
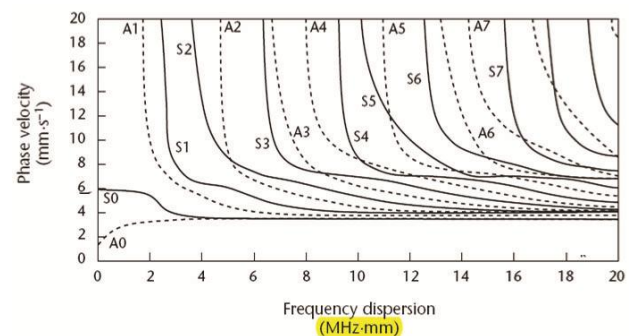

Figure 3. Phase velocity dispersion curves for Lamb waves in an aluminum plate

Although the dispersion diagrams are complex, they can be simplified using the incidence angle of the excited wave to determine which mode is dominant. A particular Lamb wave can be excited if the phase velocity of the incident longitudinal wave is equal to the phase velocity of the particular mode. A Lamb wave created by a piezoelectric sensor at a specified frequency has a particular group velocity which can be determined by measuring the TOF in the specimen using appropriate devices to detect the signal properties. TOF

information can be utilized to locate defective sources or spots in a testing sample or a specimen by verifying the distortion of the waves between the actuator and a signal-receiving sensor. The group velocity of the Lamb waves mainly depends on a structure's resonant frequency and operation modes; therefore, as the waves propagate across an area of the specimen far away, the waves slow down [15]. The localization of Lamb wave dispersion curves while eliminating spurious components can be achieved by combining a differential reassignment procedure with non-linear anisotropic diffusion [16]. An experimental and analytical survey of candidate methods for in-situ damage detection in composite materials was presented in [17]. Other information that can be used for source localization is the part of a wave which is reflected proportionally to the inhomogeneities from the sample's stiffness and density. Source localization can be achieved by correlating this information.

III. METHOD

III.I Modeling Approach

Finite element modeling based on a configuration of piezoelectric sensors was conducted using the commercial software ABAQUS. The configuration is shown in Fig. 4.
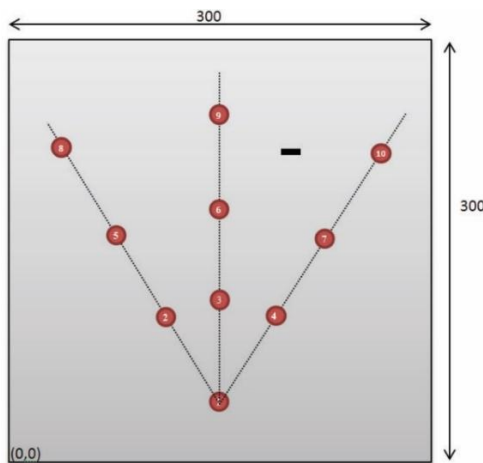

Figure 4. Configuration of the sensors and defect for the modeling simulation

An isotropic aluminum plate with a thickness of 2 *mm* was modeled with three-dimensional elements. Ideally bonded circular sensors with a radius of 4 *mm* were positioned on the plate. Sensor 1 was fixed as the actuator and the through-thickness displacement signal was collected at the center of Sensors 2 to 10 so that both the pitch-catch and pulse-echo configurations were measured. Measuring the through-thickness displacement means that A_0 is the dominant mode, which would simplify the signal processing for TOF calculations. Modeling was first performed on a configuration without any defects, after which a 20×10 *mm* through-hole defect was introduced (Fig. 4). The generated signals collected by Sensors 2, 6, and 10 are displayed in Fig. 5. All of the signals contained damage information. The excitation signal used in this configuration was a five-cycle Hanning window with a 175 *kHz* center frequency and a velocity of 2420 *m/s*.
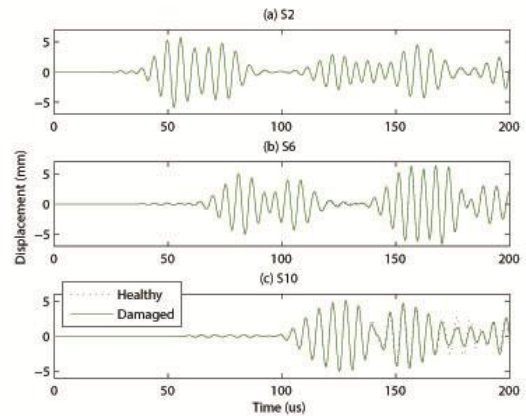

Figure 5. Signals generated from the modeling approach at (a) Sensor 2, (b) Sensor 6, and (c) Sensor 10

This signal was applied as a concentrated force at each node at the edge of the sensors to reflect the behavior of an ideally bonded piezoelectric wafer. The signal collected at Sensor 7 for the configuration and responses collected before and after the introduction of the damage is presented in Fig. 6 (a).
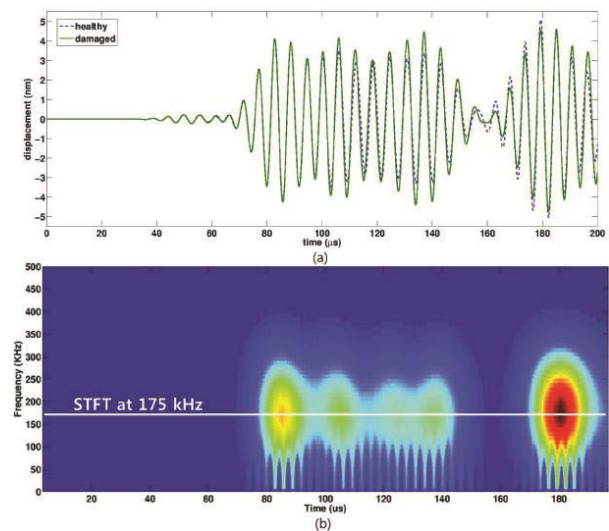

Figure 6. Modeled signal and its short time Fourier transform (STFT): (a) generated signal at Sensor 7 and (b) the STFT of the signal

To calculate the TOF of the wave reflected from the defect, a single peak representing defect scattering needed to be obtained. To achieve this, the baseline signal was subtracted from the damage signals to acquire a signal for damage scattering only. A short time Fourier transform (STFT) was used to obtain this; Figure 6(b) presents the STFT for the signal. The line corresponding to the center excitation frequency was then used to acquire the energy time profile at this frequency. The time of the first peak in Fig. 7 corresponds to the TOF of the wave from the actuator to the defect and then to the sensor. The other peaks correspond to reflections from the edges and are not of interest. The *x* and *y* coordinates of the sensors, the measured TOF from the sensors to the defect, and the calculated physical distance based on velocity effects are listed in Table 1.
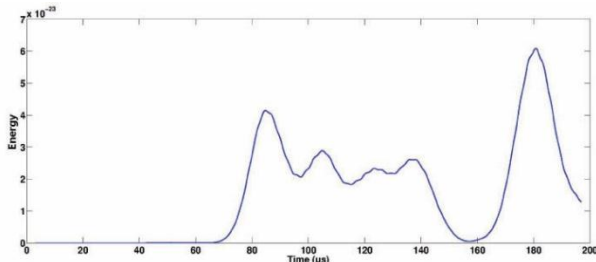
Figure 7. STFT line profile at 175 kHz.

Table 1. Sensor and defect location and TOF (µs) and distance information for the model configuration

Sensors	$x(cm)$	$y(cm)$	TOF	$D(cm)$
1	15	3	81.32	19.67
2	11	9.92	55.63	13.46
3	15	11	54.73	13.24
4	19	9.92	49.93	12.08
5	7	16.85	64.93	15.71
6	15	19	33.78	8.17
7	23	16.85	21.28	5.14
8	3	23.78	76.63	18.54
9	15	27	59.73	14.45
10	27	23.78	26.83	6.49
Damage	21	21.4	0	0

III.II EXPERIMENTAL SETUP AND MEASUREMENTS OF TOF WITH WAVE VELOCITY

In order to test the proposed source localization approach, experiments were also carried out for signal acquisition from a test specimen. Figure 8 presents the experimental setup with corresponding images.
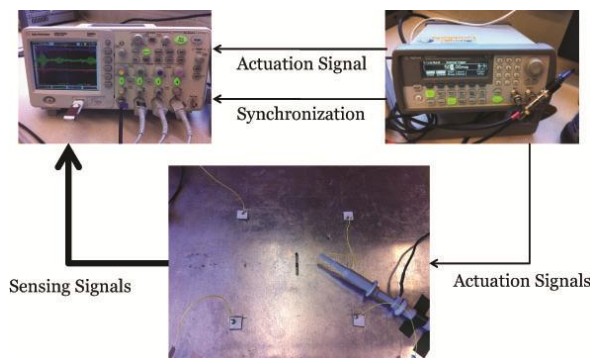

Figure 8. Block diagram and images of the experimental setup

Actuation and synchronization signals were generated using a function generator connected to an oscilloscope. The actuation sensor, which was connected to the function generator, generated Lamb waves and three additional sensors acquired signals from inhomogeneities around them. The signals were displayed in the oscilloscope using three channels at once and saved in flash memory for further processing. Square 10×10-mm PZT patches were used for actuation and sensing. The actuation signal was a 5-cycle sine wave tone burst and the frequency was set to 430 *kHz*. Lamb waves have at least two modes at any given frequency. In this experiment, the signals

operated in *A_0*, *A_1*, and *S_0* modes at the same time. Mode response depended on the excitation frequency, and the wave velocity ranged between 2700 *m/s* and 3000 *m/s*. The specimen had dimensions of 60 *cm* × 60 *cm* and a thickness of 4 *mm* as shown in Fig. 9.
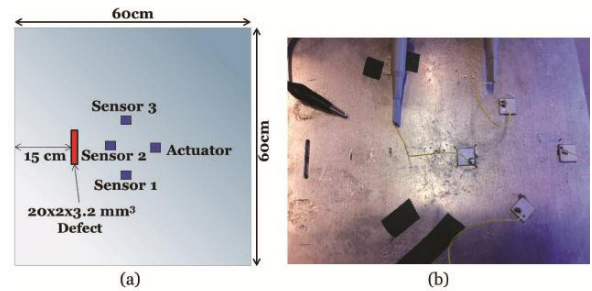

Figure 9. Dimensions of the defect and the test specimen: (a) graphic configuration and (b) image of the setup

A defect with the dimensions $20 \times 2 \times 3.2$ *mm³* was positioned 15 *cm* away from the edge of the specimen. Fig. 9(a) shows the experimental geometry of the defect in the specimen, and (b) shows an image of the experimental setup with the four PZT sensors (one for actuation and three for sensing) and the defect of the left side. One set of ultrasonic Lamb wave signals obtained from the experiment is displayed in Fig. 10.

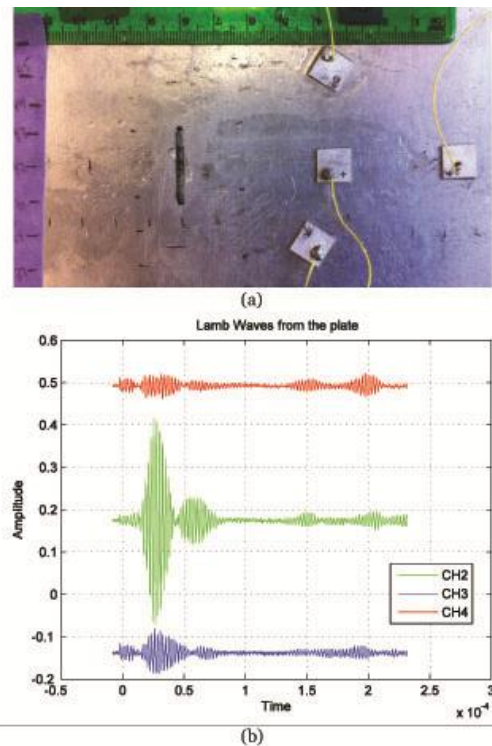**Figure 10.** Ultrasonic Lamb waves obtained from Experimental Setup 1 from Table 1: (a) Image of the sensor arrangement and (b) signals obtained from each of the three channels

Fig. 10(a) presents an image of the setup with sensors and Fig. 10(b) shows the experimentally acquired Lamb wave signals corresponding to each of the three sensors located on the left of the actuator, which is located alone on the right side of the

aluminum plate. The sensor located in the middle corresponds to Channel 2 and the lowermost and uppermost sensors correspond to Channels 3 and 4, respectively. The signal is from one of four different sensor arrangements. Each of them has three waves from three different channel outputs and these are used to obtain the TOF for the actuator, three sensors, and the defect. The signal from Channel 2 was the clearest from the defect source which is the second biggest signal amplitude's changing part because it was aligned in a direct line with the defect and the actuator, so the wave from the actuator traveled directly to the defect without any obstructions. The first peak from the sensor itself was produced when it met the waves from the actuator for the first time. The other peaks could be from the edges of the specimen, other obstacles, or previously undiscovered inhomogeneities. In order to gather information for source localization, estimating the TOF between the actuator and the sensor itself is required to compute the velocity of the waves. The TOF was estimated by determining the position of the peak value from the signal, and the wave velocity calculated as

$$V_w = \frac{S_{AS}}{T_{AS}} \tag{3}$$

where V_w is the wave velocity and T_{AS} and S_{AS} are the time and physical distance between the actuator and the sensor, respectively. S_{AS} was already known because the positions of the two sensors were known. In the next step, the TOF between the sensor and the defect (T_{SD}) was calculated. This was also obtained from the estimation of the position of the peak value. The distance between the sensor and the defect S_{SD} can be obtained using equation (4):

$$S_{SD} = V_W \times T_{SD} \tag{4}$$

Table 2 presents the estimated T_{SD} and S_{SD} between the sensor and the defect for the three channels of the four configurations.

Table 2. The measured TOF T_{SD} (μs) and estimated distance S_{SD} (cm) from the experiment

Channel	1		2		3		4	
	T_{SD}	S_{SD}	T_{SD}	S_{SD}	T_{SD}	S_{SD}	T_{SD}	S_{SD}
1	18.1	3.67	16.6	3.65	14.9	3.56	12.5	2.97
2	21.4	4.62	20.2	5.45	24.8	5.18	18.3	4.99
3	17.5	4.22	12.7	3.46	11.7	3.21	20.5	5.39

The physical distance information S_{AS} and S_{SD} needs to be formatted because the source localization process operates in an x and y axis coordinate environment on a centimeter scale. S_{SD} is used in the optimization process of an LMS algorithm to determine the best estimation of the location of the defect.

IV. SOURCE LOCALIZATION USING LMS

IV.I Distance and MSE Computations
The measured distance between the sensor and the defect from the modeling and experiments was used in the LMS process. The MSE between the measured and the actual values of the distance between the sensor and the defect was computed and used in LMS signal processing. Figure 11 displays the geometry of the defect $D(x_D, y_D)$ and the three sensors $S_1(x_{s_1}, y_{s_1})$, $S_2(x_{s_2}, y_{s_2})$, and $S_3(x_{s_3}, y_{s_3})$ around it.
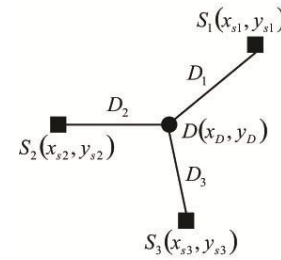

Figure 11. Geometry of defect D and the three sensors S_1, S_2, and S_3

The actual distance between each sensor and the defect can be easily obtained using the Euclidean distance principle. D_1, D_2, and D_3 are the distances between D and S_1, S_2, and S_3, respectively; these were calculated using equation (5).

$$D_i = \sqrt{\left(x_{s_i} - x_D\right)^2 + \left(y_{s_i} - y_D\right)^2} \quad (i = 1,2,3) \tag{5}$$

The distances D_{m_1}, D_{m_2}, and D_{m_3} between the defect and each of the three sensors measured from the experiment were used to calculate the MSE, which represents the error between the theoretical and experimental distances. D_{m_i}, where $i = 1, 2,$ or 3, was derived from the computation of S_{SD} in equation (4). The MSE (E) between D_i and D_{m_i} can be written as

$$E = \frac{1}{N} \sum_{i=1}^{N} \left(D_i - D_{m_i}\right)^2 \quad (N = 3) \tag{6}$$

The MSE needs to be minimized to determine the optimal position of the defect $D(x_D, y_D)$ by taking the partial derivative of E with respect to x_D and y_D, respectively, and moving in the opposite direction to the gradient of E.

IV.II Mathematical Formulation for the Gradient of Error
LMS algorithms are widely used in a number of applications due to their computational simplicity and effectiveness [18]. The LMS method was used to arrive at estimates of x and y coordinates for a defect (x_D and y_D, respectively). The gradient of MSE was employed to estimate x_D and y_D. Because E can be written as

$$E = E_1 + E_2 + E_3 \tag{7}$$

the gradient of E is given by

$$\nabla E = \nabla E_1 + \nabla E_2 + \nabla E_3$$
$$= \frac{1}{3}\left[\nabla\left(D_1 - D_{m_1}\right)^2 + \nabla\left(D_2 - D_{m_2}\right)^2 + \nabla\left(D_3 - D_{m_3}\right)^2\right] \tag{8}$$

As explained previously, x_D and y_D need to be estimated. In order to accomplish this, it was necessary to calculate the gradient of E by taking the partial derivative of E with respect to x_D and y_D. $\frac{\partial E}{\partial x_D}$ can be obtained using

$$\frac{\partial E}{\partial x_D} = \frac{1}{3}\begin{bmatrix} 2\left(D_1 - D_{m_1}\right)\frac{\partial D_1}{\partial x_D} + \\ 2\left(D_2 - D_{m_2}\right)\frac{\partial D_2}{\partial x_D} + 2\left(D_3 - D_{m_3}\right)\frac{\partial D_3}{\partial x_D} \end{bmatrix} \tag{9}$$

In equation (9), $\frac{\partial D_1}{\partial x_D}$ can be written as

$$\begin{aligned}
\frac{\partial D_1}{\partial x_D} &= \frac{\partial}{\partial x_D}\left[\left(x_{s_1} - x_D\right)^2 + \left(y_{s_1} - y_D\right)^2\right]^{\frac{1}{2}} \\
&= \frac{1}{2}\left[\left(x_{s_1} - x_D\right)^2 + \left(y_{s_1} - y_D\right)^2\right]^{-\frac{1}{2}} \times \\
&\quad \frac{\partial}{\partial x_D}\left[\left(x_{s_1} - x_D\right)^2 + \left(y_{s_1} - y_D\right)^2\right] \\
&= \frac{1}{2}D_1^{-1} \times \begin{bmatrix} 2\left(x_{s_1} - x_D\right)\frac{\partial}{\partial x_D}\left(x_{s_1} - x_D\right) + \\ 2\left(y_{s_1} - y_D\right)\frac{\partial}{\partial x_D}\left(y_{s_1} - y_D\right) \end{bmatrix} \\
&= \frac{1}{2}D_1^{-1} \times \left[2\left(x_{s_1} - x_D\right)(0 - 1) + 2\left(y_{s_1} - y_D\right)(0 - 0)\right] \\
&= -D_1^{-1}\left(x_{s_1} - x_D\right) \tag{10}
\end{aligned}$$

In the same way, $\frac{\partial D_2}{\partial x_D}$ and $\frac{\partial D_3}{\partial x_D}$ can also be obtained as

$$\frac{\partial D_2}{\partial x_D} = -D_2^{-1}\left(x_{s_2} - x_D\right) \tag{11}$$

$$\frac{\partial D_3}{\partial x_D} = -D_3^{-1}\left(x_{s_3} - x_D\right) \tag{12}$$

Following this, $\frac{\partial E}{\partial x_D}$ can be obtained by inserting equations (10), (11), and (12) into equation (9), finally resulting in

$$\frac{\partial E}{\partial x_D} = -\frac{2}{3}\begin{bmatrix} \left(1 - D_{m_1}D_1^{-1}\right)\left(x_{s_1} - x_D\right) + \\ \left(1 - D_{m_2}D_2^{-1}\right)\left(x_{s_2} - x_D\right) + \\ \left(1 - D_{m_3}D_3^{-1}\right)\left(x_{s_3} - x_D\right) \end{bmatrix} \tag{13}$$

Similarly, $\frac{\partial E}{\partial y_D}$ can also be calculated as

$$\frac{\partial E}{\partial y_D} = \frac{1}{3}\begin{bmatrix} 2\left(D_1 - D_{m_1}\right)\frac{\partial D_1}{\partial y_D} + \\ 2\left(D_2 - D_{m_2}\right)\frac{\partial D_2}{\partial y_D} + 2\left(D_3 - D_{m_3}\right)\frac{\partial D_3}{\partial y_D} \end{bmatrix} \tag{14}$$

In equation (14), the $\frac{\partial D_1}{\partial y_D}$ can be written as

$$\begin{aligned}
\frac{\partial D_1}{\partial y_D} &= \frac{\partial}{\partial y_D}\left[\left(x_{s_1} - x_D\right)^2 + \left(y_{s_1} - y_D\right)^2\right]^{\frac{1}{2}} \\
&= \frac{1}{2}\left[\left(x_{s_1} - x_D\right)^2 + \left(y_{s_1} - y_D\right)^2\right]^{-\frac{1}{2}} \times \\
&\quad \frac{\partial}{\partial y_D}\left[\left(x_{s_1} - x_D\right)^2 + \left(y_{s_1} - y_D\right)^2\right] \\
&= \frac{1}{2}D_1^{-1} \times \begin{bmatrix} 2\left(x_{s_1} - x_D\right)\frac{\partial}{\partial y_D}\left(x_{s_1} - x_D\right) + \\ 2\left(y_{s_1} - y_D\right)\frac{\partial}{\partial y_D}\left(y_{s_1} - y_D\right) \end{bmatrix} \\
&= \frac{1}{2}D_1^{-1} \times \left[2\left(x_{s_1} - x_D\right)(0 - 0) + 2\left(y_{s_1} - y_D\right)(0 - 1)\right] \\
&= -D_1^{-1}\left(y_{s_1} - y_D\right) \tag{15}
\end{aligned}$$

In the same way, $\frac{\partial D_2}{\partial y_D}$ and $\frac{\partial D_3}{\partial y_D}$ also can be obtained as

$$\frac{\partial D_2}{\partial y_D} = -D_2^{-1}\left(y_{s_2} - y_D\right) \tag{16}$$

$$\frac{\partial D_3}{\partial y_D} = -D_3^{-1}\left(y_{s_3} - y_D\right) \tag{17}$$

Finally, $\frac{\partial E}{\partial y_D}$ can be obtained by inserting equations (15), (16), and (17) into equation (14), resulting in

$$\frac{\partial E}{\partial y_D} = -\frac{2}{3}\begin{bmatrix} \left(1 - D_{m_1}D_1^{-1}\right)\left(y_{s_1} - y_D\right) + \\ \left(1 - D_{m_2}D_2^{-1}\right)\left(y_{s_2} - y_D\right) + \\ \left(1 - D_{m_3}D_3^{-1}\right)\left(y_{s_3} - y_D\right) \end{bmatrix} \tag{18}$$

The obtained values of $\frac{\partial E}{\partial x_D}$ and $\frac{\partial E}{\partial y_D}$ were then employed in the steepest descent method outlined in the next section.

IV.III Error Minimization using the Gradient Descent Algorithm

The gradient descent algorithm (also known as the steepest descent algorithm) is an efficient method because it works with true gradient vectors rather than estimates. Therefore, the performance of other gradient algorithms can at most be close to the performance of the steepest descent method [19][20]. Using this iterative minimization procedure, the optimal values of x_D and y_D which result in the minimum error can be achieved by orienting the search in a direction that is opposite to that of the gradient of E, which defines the direction of maximum increase. The steepest descent algorithm updates the coefficients using

$$\vartheta_{i+1} = \vartheta_i - \epsilon \frac{\partial F(\vartheta)}{\partial \vartheta}\bigg|_{\vartheta = \vartheta_i} \tag{19}$$

Because $\nabla_\vartheta F$ defines the direction of maximum increase in the function, the function $F(\vartheta)$ can be minimized by recursively calculating $\nabla_\vartheta F$ and adjusting ϑ until it reaches a minimum. ε is the convergence factor because it affects convergence behavior. The algorithm for minimizing a function can be summarized as follows:

(a) Make the initial guess ϑ_0

(b) Compute $\nabla_\vartheta F$, that is,

$$\frac{\partial F(\vartheta_0)}{\partial \vartheta} \tag{20}$$

(c) Adjust ϑ_0 to obtain ϑ_1 by moving in a direction opposite to the gradient, that is,

$$\vartheta_1 = \vartheta_0 - \varepsilon \left[\frac{\partial F(\vartheta_0)}{\partial \vartheta}\right] \tag{21}$$

(d) Stop when $\vartheta_{i+1} - \vartheta_i$ is sufficiently small.

This minimization procedure can be applied to minimize E. x_D and y_D were estimated recursively as follows:

$$x_{D_{i+1}} = x_{D_i} - \varepsilon \left. \frac{\partial E}{\partial x_D} \right|_{x_D = x_{D_i}} \quad (22)$$

$$y_{D_{i+1}} = y_{D_i} - \varepsilon \left. \frac{\partial E}{\partial y_D} \right|_{y_D = y_{D_i}} \quad (23)$$

$\frac{\partial E}{\partial x_D}$ and $\frac{\partial E}{\partial y_D}$ in equations (22) and (23) can be calculated using analytical solutions (equations 13 and 18, respectively). They can also be computed numerically

$$x_{D_{i+1}} = x_{D_i} - \varepsilon \frac{E|_{x_D = x_{D_i} + \Delta x_D, y_D = y_{D_i}} - E|_{x_D = x_{D_i}, y_D = y_{D_i}}}{\Delta x_D} \quad (24)$$

$$y_{D_{i+1}} = y_{D_i} - \varepsilon \frac{E|_{x_D = x_{D_i}, y_D = y_{D_i} + \Delta y_D} - E|_{x_D = x_{D_i}, y_D = y_{D_i}}}{\Delta y_D} \quad (25)$$

by choosing appropriately small values of Δx_D and Δy_D. The iteration process should stop, if and only if, $|x_{D_{i+1}} - x_{D_i}|$ and $|y_{D_{i+1}} - y_{D_i}|$ are sufficiently small. Using this optimization procedure, x_D and y_D are obtained. Results obtained using this procedure are presented in the next section.

V. RESULTS

V.I Results from the Modeled Signals
To test and verify the proposed source localization system, an application program was implemented using MATLAB 7.0. Figure 12 shows the application program and its output for the LMS signal processing used to optimize x_D and y_D.
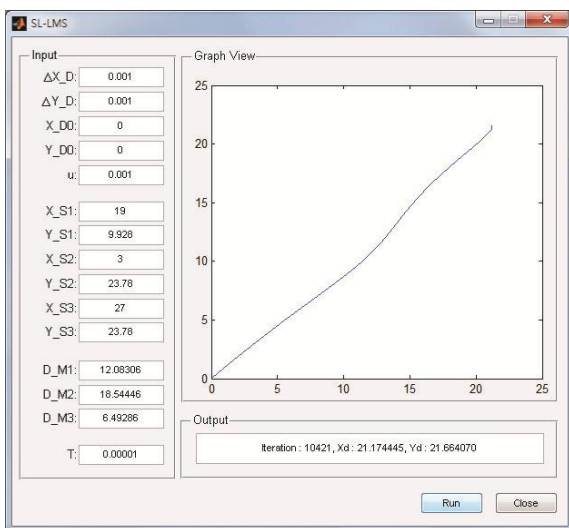

Figure 12. MATLAB R2018b application program for source localization iteration

The input values for the application program are the three sensor positions and the corresponding estimates for TOF, Δx_D, and Δy_D, and the initial values of x_D and y_D, the convergence factor, and a threshold value used to determine when to stop the gradient descent iteration process. The line starts from the position (0,0) and searches for the optimal position of x_D and y_D, leaving a trace. The trajectory follows the x and y positions

which give the minimum error and are in the opposite direction of the gradient of E for the difference between the actual and estimated distance between the sensor and the defect. The output from the program, which is the iteration number and the final optimized values of x_D and y_D, is displayed under the graph. Table 3 shows the optimal values of x_D and y_D produced by the gradient descent algorithm.

Table 3. Optimally estimated values of x_D and y_D for eight cases from the modeling process (Actual $x_D = 21$, $y_D = 21.4$, HR = hit rate)

Sensor Numbers	x_D(HR)	y_D(HR)
S1, S8, S10	21.21(99%)	21.52(99.44%)
S4, S5, S7	21.88(95.81%)	21.77(98.27%)
S1, S7, S8	21.37(98.24%)	21.67(98.74%)
S5, S8, S10	21.55(97.39%)	21.01(98.18%)
S1, S5, S7	21.81(96.15%)	21.69(98.64%)
S7, S8, S10	21.14(99.33%)	21.51(99.49%)
S4, S8, S10	21.17(99.19%)	21.66(98.79%)
S6, S7, S10	21.71(96.62%)	21.87(97.8%)
Average HR	97.72%	98.67%

These values are composed of the estimated *x* and *y* coordinates for the defect for each of eight cases. The averaged hit ratio for the *x* and *y* coordinates in this case is 97.72% and 98.67%, respectively.
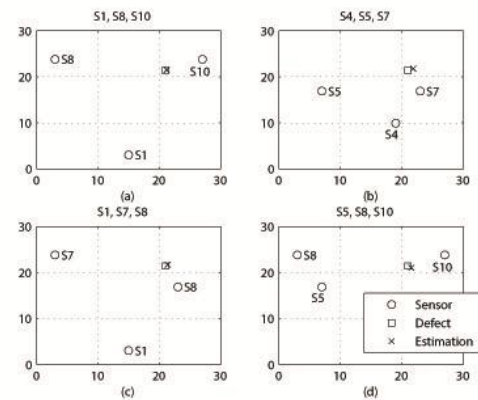

Figure 13. Source localization results for the modeled signals with sensors: (a) S_1, S_8, and S_{10}, (b) S_4, S_5, and S_7, (c) S_1, S_7, and S_8, and (d) S_5, S_8, and S_{10}
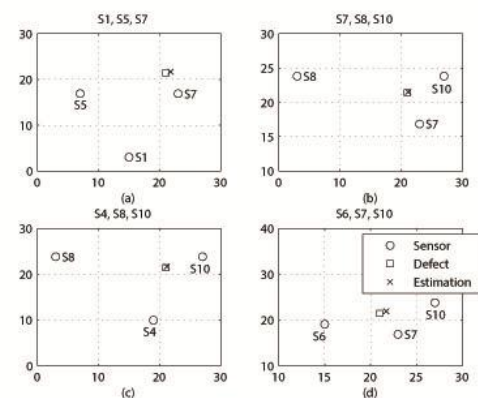

Figure 14. Source localization results for the modelled signals with sensors: (a) S_1, S_5, and S_7, (b) S_7, S_8, and S_{10}, (c) S_4, S_8, and S_{10}, and (d) S_6, S_7, and S_{10}

In order to determine the validity of these results, the optimally estimated values of x_D and y_D are plotted in Fig. 13 and Fig. 14 with the presence of the defect and the sensors used in the modeling stage. In these figures, the circle, cross, and square represent the location of the sensor and the estimated and actual location of the defect, respectively. The sensors used to estimate the location of the defect are titled to each of pictures in Fig. 13 and Fig. 14. It can be observed that the estimated positions of the defect are reasonably close to the actual positions.
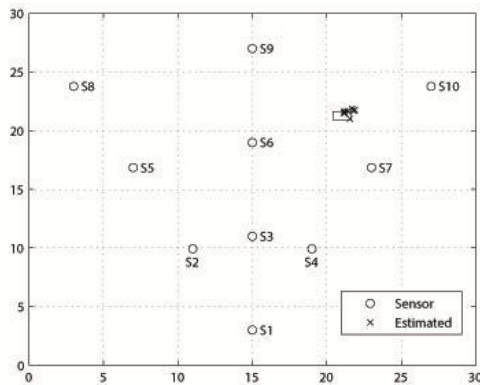

Figure 15. Plot of the source localization results for all eight modeled signals

Figure 15 shows the plot for all sensors (circles) with the eight estimated results (crosses) together and the real position of the defect (rectangles). From Fig. 15, it can also be seen that the optimally estimated positions of the defect are close to the actual location.

V.II Results from the Experimental Signals
Table 4 shows the optimal values of x_D and y_D based on the application of the gradient descent algorithm using the distance information from the experiments.

Table 4. Optimally estimated values of x_D and y_D coordinates for four cases from the experiment (A = actual, E = estimated, HR = hit rate)

Case	A		E	
	x_D	y_D	x_D(HR)	y_D(HR)
1	3	3	3.81(73%)	3.51(83%)
2	4	5	4.42(89.5%)	5.25(95%)
3	4	6	4.36(91%)	6.45(92.5%)
4	4	4	4.43(89.3%)	3.04(76%)
Average			85.68%	86.63%

These values are composed of the actual and estimated *x* and *y* coordinates of the defect for each of four cases. The average hit rate for the *x* and *y* coordinates was 85.68% and 86.63%, respectively, which was lower than for the modeling. This may be due to more inaccurate measurement of the TOF and the distance between the defect and the sensor in the experimental environment. For the purpose of verification, the optimally estimated values of x_D and y_D were also positioned in Fig. 16 and Fig. 17 with the existence of the defect. The white spot represents the estimated location of the defect based on the LMS iteration and indicates the final result of source localization signal processing. Lines are included to clarify the dimensions of the specimen and it spaces 1 *cm* every line in between for horizontal and vertical directions at the same time.
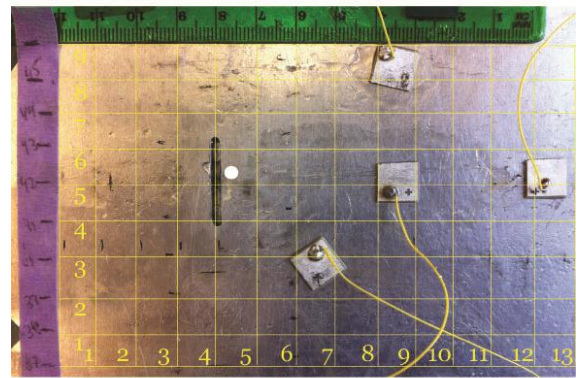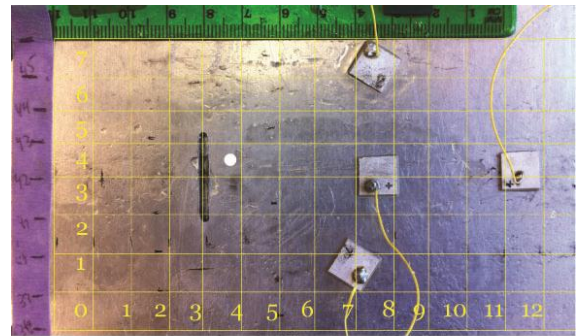

Figure 16. Source localization results for the experimental signals: (a) Case 1 and (b) Case 2
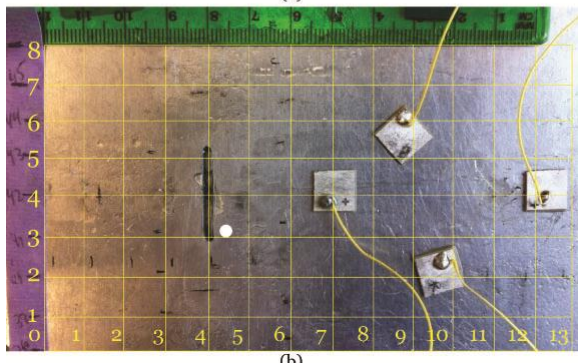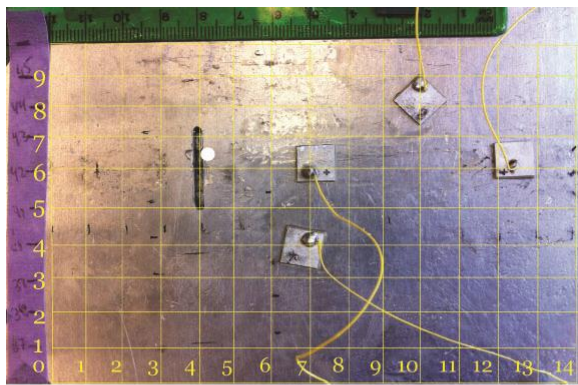

Figure 17. Source localization results for the experimental signals: (a) Case 3 and (b) Case 4

The rightmost sensor is the actuator and the others act as receiving sensors. Because the defect is rectangular, the center point is set to the coordinate location of the defect for the best optimization. As with the modeling approach, the estimation results were reasonably consistent with the actual position of the defect source. In order to verify the source localization system proposed in this study, we tested the signal processing algorithm using the actual distances between the sensors and the defect to determine if the optimized output results x_D and y_D exhibited a reasonably good match to the real defect coordinates in the testing environment. Table 5 displays the verification results for the cases.

Table 5. Verification results for x_D and y_D for the modeling and experiments

Modelling		
Sensor Number	x_D(HR)	y_D(HR)
S1, S8, S10	21.00(100%)	21.38(99.91%)
S4, S5, S7	21.01(99.95%)	21.39(99.95%)
S1, S7, S8	20.98(99.9%)	21.39(99.95%)
S5, S8, S10	21.01(99.95%)	21.30(99.53%)
S1, S5, S7	20.98(99.9%)	21.40(100%)
S7, S8, S10	20.99(99.95%)	21.38(99.91%)
S4, S8, S10	21.00(100%)	21.38(99.91%)
S6, S7, S10	21.00(100%)	21.38(99.91%)
Average HR	99.96%	99.88%
Experiments		
Case	x_D(HR)	y_D(HR)
1	3.00(100%)	2.97(99%)
2	3.99(99.75%)	4.98(99.6%)
3	3.99(99.75%)	5.96(99.33%)
4	4.00(100%)	3.93(98.25%)
Average HR	99.88%	99.05%

The optimized output results for locating the defect were a good match to the actual *x* and *y* coordinates of the defect in the testing specimen. The average hit ratio for the *x* and *y* coordinates was 99.96% and 99.88% for the modeling and 99.88% and 99.05% for the experiments, respectively. This means that the LMS signal processing system proposed in this research operates as intended and that more precisely estimated TOF would produce more accurate estimation results for the source localization of a defect.

VI. CONCLUSION

A novel approach to source localization using ultrasonic Lamb wave signals in NDE has been described in this paper. The method uses an LMS algorithm to estimate the position of a defect. The results obtained through modeling and physical experiments were compared and analyzed. The proposed method for estimating the location of a defect in a specimen employed an *x-y* plane coordinate system and an LMS algorithm. The distance between the sensor and the defect was measured from the collected data using the position of the peak value, the TOF, and velocity effects. Equations for the gradient of the MSE with respect to the desired x and y position of the source were derived and minimized to produce the most accurate estimation results. It was found that the more precise the TOF information, the better the results. Therefore, another

method for measuring TOF more accurately could be applied to improve source localization using ultrasonic Lamb waves. In order to improve the accuracy and speed of the process, another least squares method, such as a Newton-Raphson algorithm, which is a second-order method, can be applied to generate faster convergence and more accurate *x* and *y* coordinates for the defect source. For further research, circular-shaped materials should also be considered for 3-dimensional source localization, for which cylindrical or spherical coordinates will need to be employed.

REFERENCES

[1] Viktorov IA. Rayleigh and Lamb Waves. Physical Theory and Applications. New York: Plenum Press. 1967.

[2] Giurgiutiu V, Cuc A. Embedded Non-destructive Evaluation for Structural Health Monitoring, Damage Detection, and Failure Prevention. The Shock and Vibration Digest. 2005;37(2):83-105.

[3] Mahato PK, Sen S. Effect of surface modification of ceramic particles by SDS on the electrical properties of PZT-PVDF and BT-PVDF composites: interface effect. Journal of Materials Science: Materials in Electronics. 2015;26(5):2969-2976.

[4] Giurgiutiu V. Lamb Wave Generation with Piezoelectric Wafer Active Sensors for Structural Health Monitoring. Proc. SPIE's Annual Int. Sympo. on Smart Structures and Materials and 8th Annual Int. Sympo. on NDE for Monitoring and Diagnostics. 2002:paper#5056-17.

[5] Giurgiutiu V. Tuned Lamb Wave Excitation and Detection with Piezoelectric Wafer Active Sensors for Structural Health Monitoring. Jour. Intell. Mater. Syst. Struct. 2005;16:291-305.

[6] Xu E, Ding Z, Dasgupta S. Source Localization in Wireless Sensor Networks From Signal Time-of-Arrival Measurements. IEEE Trans. Signal Process. 2011;59(6):2887-2897.

[7] Herrmann S, Wellnitz J, Jahn S, Leonhardt S. Structural Health Monitoring for Carbon Fiber Resin Composite Car Body Structures. Proceedings of the 5th International Conference ICSAT. 2013:75-96.

[8] Rokhlin SI, Kim JY, Xie B, Zoofan B. Nondestructive Sizing and Localization of Internal Microcracks in Fatigue Samples. NDT & E International. 2007;40(6):462-470.

[9] Jiang J, Duan F, Li YC, Hua XN. Localization of 3D near-field source using the aperture extension method and nonuniform cross array. Progress In Electromagnetics Research B. 2013;55(55):297-324.

[10] Chlada M, Blahacek M, Prevorovsky Z. AE Source Location by Neural Networks with Arrival Time

Profiles. Proc. NDT in Progress, 5th Int. Work. NDT Experts. 2009:11-18.

[11] Baskaran R, Janawadkar MP. Defect localization by orthogonally projected multiple signal classification approach for magnetic flux leakagefields. NDT & E International. 2008;41(6):416-419.

[12] Reed CW, Hudson R, Yao K. Direct Joint Source Localization and Propagation Speed Estimation. Proc. IEEE Int. Conf. Acoust., Speech, Signal Process. (ICASSP), 1999;3:1169-1172.

[13] Yardibi T, Li J, Stoica P, Xue M, Baggeroer AB. Source Localization and Sensing: A Nonparametric Iterative Adaptive Approach Based on Weighted Least Squares. IEEE Trans. Aerosp. Electro. Sys. 2010;46(1):425-443.

[14] Manka M, Rosiek M, Martowicz A, Uhl T, Stepinski T. Design and simulations of Interdigital Transducers for Lamb-wave based SHM systems. 11th IMEKO TC 10 Workshop on Smart Diagnostics of Structures, Krakow. 2010.

[15] Kessler SS, Spearing SM, Soutis C. Damage detection in composite materials using Lamb wave methods. Smart Materials and Structures. 2002;11(2):269-278.

[16] Kotte O, Niethammer M, Jacobs LJ. Lamb Wave Characterization by Differential Reassignment and Nonlinear Anisotropic Diffusion. NDT & E International. 2006;39(2):96-105.

[17] Kessler SS, Spearing SM, Soutis C. Optimization of Lamb Wave Methods for Damage Detection in Composite Materials. Proc. 3rd Int. Work. Struct. Health Monitor. 2001:870-879.

[18] Lefteris T. Adaptive Filtering : Theories and Applications, Scitus Academics LLC. 2016.

[19] Uncini A. Fundamentals of Adaptive Signal Processing. Springer. 2015.

[20] Beyerer J. Pattern Recognition: Introduction, Features, Classifiers and Principles. Walter de Gruyter. 2017.